Research Square

Preprints are preliminary reports that have not undergone peer review.
They should not be considered conclusive, used to inform clinical practice,
or referenced by the media as validated information.

# High harmonic generation reflecting the sub-cycle evolution of the Mott transition under a mid-infrared electric field

**Hiroshi Okamoto**

okamotoh@k.u-tokyo.ac.jp

University of Tokyo https://orcid.org/0000-0003-2807-5277

**Ryohei Ikeda**

University of Tokyo

**Yuta Murakami**

Tohoku University https://orcid.org/0000-0001-5200-0019

**Daiki Sakai**

University of Tokyo

**Tatsuya Miyamoto**

Nagoy Institute of Technology

**Toshimitsu Ito**

National Institute of Advanced Industrial Science and Technology https://orcid.org/0000-0003-2094-2807

**Article**

**Keywords:**

**Posted Date:** September 29th, 2025

**DOI:** https://doi.org/10.21203/rs.3.rs-7287112/v1

**License:** This work is licensed under a Creative Commons Attribution 4.0 International License.
Read Full License

**Additional Declarations:** There is **NO** Competing Interest.

**Version of Record:** A version of this preprint was published at Nature Photonics on November 13th, 2026. See the published version at https://doi.org/10.1038/s41566-026-02031-w.

# High harmonic generation reflecting the sub-cycle evolution of the Mott transition under a mid-infrared electric field

Ryohei Ikeda[1], Yuta Murakami[2,3], Daiki Sakai[1], Tatsuya Miyamoto[1,4], Toshimitsu Ito[5], Hiroshi Okamoto[1]

[1]*Department of Advanced Materials Science, University of Tokyo, Chiba 277-8561, Japan*

[2]*Institute for Materials Research, Tohoku University, Sendai 980-8577, Japan*

[3]*Center for Emergent Matter Science, RIKEN, Wako, Saitama 351-0198, Japan*

[4]*Department of Engineering, Nagoya Institute of Technology, Nagoya, 466-8555, Japan*

[5]*National Institute of Advanced Industrial Science and Technology, Tsukuba 305-8565, Japan*

**Solids in an intense laser field show high-harmonic generation (HHG), which can provide information on carrier dynamics and band structures in weakly correlated systems. In strongly correlated systems, a laser field can induce a transition between the various electronic phases formed by the entanglement of charge, spin, and orbital degrees of freedom via carrier generation. The HHG accompanying this process should contain information on the nonequilibrium electronic-state dynamics along the oscillating field—an aspect that remains unresolved to date. Here, we show that an intense mid-infrared (MIR) pulse induces a Mott insulator–metal transition in a one-dimensional cuprate, $Sr_2CuO_3$, the evolution of which is reflected by the spectral features of HHs. When the electric-field amplitude exceeds 6 MV/cm, carriers are efficiently generated and each harmonic frequency decreases from odd multiples of the MIR frequency. Dynamical mean-field theory indicates that these redshifts originate from a series of electronic-structure reconstructions in each electric-field cycle during the melting of the Mott-insulator state, which modifies the radiation phase from carrier recombination cycle-by-cycle. This phenomenon is negligible in rigid-band systems. This experimental-theoretical study confirms that HH spectroscopy research can potentially unravel the sub-cycle dynamics of nonequilibrium phase transitions in correlated materials.**

High harmonic generation (HHG), a nonperturbative nonlinear optical phenomenon originating from charge dynamics under an intense light field[1,2], was initially observed in atomic and molecular gases and utilised to produce attosecond pulses[3,4] and probe attosecond-scale electron dynamics[5,6]. Subsequently, the scope of HHG research has expanded to semiconductors[7-10] and semimetals[11,12]. HHG, which is closely related to the band structure, enables band dispersion[13-15], Berry curvature[16,17], and dipole matrix element[18] analyses through HH spectral measurements in weakly correlated systems with rigid-band structures. Here, we aim to extract information on dynamic electronic-state changes, rather than static band structures, from HHG, focusing on strongly correlated systems.

In strongly correlated systems, couplings between the charge, spin, and orbital degrees of freedom often result in multiple competing ordered phases[19]. Capturing the dynamics of these degrees of freedom during phase transitions remains an important challenge. To date, this challenge has been addressed with a pump–probe setup[20-25] where the pump pulse with a photon energy exceeding the band gap generates charge carriers to trigger a phase transition, and the probe pulse detects its evolution. Recently, strong sub-gap excitation with a mid-infrared (MIR) pulse, which can create carriers through nonlinear excitation processes and induce phase transitions, has become available[26,27]. Intense MIR pump pulses also cause HHG, which reflects the dynamics of elementary excitations that emerge in strongly correlated systems[28-30]. Thus, HHG should provide, without a probe pulse, information about the ultrafast electronic-state changes or nonequilibrium phase transitions in such systems under an MIR electric field[31]. This approach is different from the previous proposals of HH spectroscopy on ultrafast phase transitions in correlated materials where HHG was simply used as a probe or measured by an advanced sub-cycle detection technique[32,33]. To clarify the features of HHG that reflect ultrafast electronic-state changes in correlated materials, we focused on a one-dimensional (1D) Mott insulator with one orbital and one electron per site. In Mott insulators, a large on-site Coulomb repulsion $U$ prevents electron motion from the singly occupied configuration, and each electron spin is arranged antiferromagnetically (Fig. 1a: lower left). The charge carriers (elementary excitations) in Mott insulators, doublons (doubly occupied sites) and holons (non-occupied sites), are created via quantum tunnelling processes under an intense sub-gap light field and give rise to Mott transitions[26,27,34-36]. Owing to spin–charge separation in a 1D system with a large $U$[37], the spectral weight of the Mott-gap transition is necessarily transferred to the Drude component[21,38] in the optical conductivity (Fig. 1a: middle). With metallisation, the electronic structure (and consequently the phase of radiation from doublon–holon recombination) is expected to change cycle-by-cycle, resulting in HH spectral changes. Here, we selected the typical 1D Mott insulator $Sr_2CuO_3$ as the target. By systematically studying the relationship between the MIR electric-field amplitude, HH spectra, and carrier density, we confirm that the sub-cycle evolution of electronic-state changes is reflected as HH shifts (Fig. 1a: lower right).

**Results**

The crystal structure of $Sr_2CuO_3$ comprises $CuO_4$ units arranged along the *b*-axis sharing two diagonal oxygen atoms to form CuO chains (Fig. 1b)[39]. Although the $d$ band created by the overlap of the copper $d_{x^2-y^2}$ orbital with the oxygen $p$ orbital is half-filled (Fig. 1c), the system is a Mott insulator because of the large Coulomb repulsion $U_\mathrm{d}$ between the $d$ electrons. The O-$2p$ band is located between the upper and lower Hubbard bands consisting of Cu-$3d$ orbital, and the system functions as a charge-transfer (CT) insulator (Fig. 1d). However, by mapping the O-$2p$ band to the lower Hubbard band, the electronic properties of this CT insulator can be discussed as those of a simple Mott insulator. In the optical conductivity ($\sigma$) spectrum of $Sr_2CuO_3$ obtained from the polarised reflectivity ($R$) spectrum along the *b*-axis (Fig. 2a), the sharp peak at 1.76 eV corresponds to the CT-gap energy, which is labelled the Mott-gap energy $\Delta_\mathrm{Mott}$ in this study. More strictly, the lowest excited state responsible for the peak is the one-photon allowed exciton[40], and a doublon-holon continuum exists slightly above it in energy[41].

On irradiating $Sr_2CuO_3$ with MIR pulses with a photon energy of $\hbar\Omega = 0.263$ eV (frequency of $\Omega/2\pi = 63.6$ THz) and a maximum amplitude $|E_\mathrm{MIR}|$ of ~4.0–12.3 MV/cm polarised along the *b*-axis, HHs polarised along the *b*-axis were detected. To exclude reabsorption and nonlinear propagation effects on HHG[42], a reflection configuration was adopted. The HHs polarised perpendicular to the *b*-axis were negligibly small (Supplementary Information S2). Figure 2b shows the HH spectra in which odd-order harmonics from the 3rd to 11th, 13th, and 15th orders are observed for $|E_\mathrm{MIR}| > 4.0,\ 5.0,$ and $8.5\ \mathrm{MV/cm}$, respectively. Because $Sr_2CuO_3$ has spatial inversion symmetry, only odd-order harmonics are observed[43]. The intensities of the harmonics decrease from the 3rd to 7th orders, remain almost constant from the 7th to 11th orders, and decrease again from the 13th order, similar to the spectral pattern of semiconductors based on the three-step model[2,7-9]. At $|E_\mathrm{MIR}| > 6.0\ \mathrm{MV/cm}$, the HH peak energies of the 5th to 13th order shift from odd multiples of $\hbar\Omega$, which reflects the Mott transition, as discussed later.

Figure 2c shows the $|E_\mathrm{MIR}|$ dependence of the integrated intensities of the $n^\mathrm{th}$-order harmonics, $I_{n\mathrm{HG}}$. For $|E_\mathrm{MIR}| < 4.0\ \mathrm{MV/cm}$, $I_{3\mathrm{HG}}$ and $I_{5\mathrm{HG}}$ follow the 6th and 10th power of $|E_\mathrm{MIR}|$ as $I_{n\mathrm{HG}} \propto |E_\mathrm{MIR}|^{2n}$, respectively, suggesting that they originate from multiphoton processes. At higher electric-field amplitudes, $I_{3\mathrm{HG}}$ is significantly enhanced, and $I_{5\mathrm{HG}}$ becomes slightly larger than the value suggested by the power-law dependence. When $|E_\mathrm{MIR}| > 7.0\ \mathrm{MV/cm}$, $I_{3\mathrm{HG}}$ and $I_{5\mathrm{HG}}$ tend to saturate. $I_{n\mathrm{HG}}$ for $n = 7-13$ do not follow the power law in the low-electric-field region, suggesting the perpetual involvement of carrier-generation processes in the HHGs. Figure 2d shows the $|E_\mathrm{MIR}|$ dependence of $I_{n\mathrm{HG}}$ normalised by the values at $|E_\mathrm{MIR}| = 12.3\ \mathrm{MV/cm}$, which are qualitatively different for $n = 3$ and $n = 7-13$, being intermediate between them for $n = 5$. Since $3\hbar\Omega$ is smaller than the original Mott-gap energy ($\Delta_\mathrm{Mott}$=1.76 eV), the deviation of $I_{3\mathrm{HG}}$

from $I_{3\mathrm{HG}} \propto |E_{\mathrm{MIR}}|^6$ is attributable to doublon–holon generations and the subsequent transient currents driven by the MIR electric field, analogous to the intraband currents in semiconductors. On the other hand, the energies of $n\hbar\Omega$ for $n \geq 7$ are larger than $\Delta_{\mathrm{Mott}}$, so that they can be ascribed to the recombination of doublons and holons generated by quantum tunnelling processes and driven by the electric field, i.e., to the three-step dynamics of doublon–holon pairs. The previous theoretical studies predict a large contribution of this phenomenon towards HHG in half-filled Mott insulators[28,29]. Since the energy of $5\hbar\Omega$ is close to the absorption edge (Fig. 2a), the deviation of $I_{5\mathrm{HG}}$ from $I_{5\mathrm{HG}} \propto |E_{\mathrm{MIR}}|^{10}$ might be attributed to the three-step dynamics of doublon-holon pairs in addition to the transient currents.

MIR pulse-induced carrier generation is expected to make Mott insulators metallic, changing the HHG mechanism. To investigate this phenomenon, evaluating the $|E_{\mathrm{MIR}}|$ dependence of the carrier density using pump-probe reflection spectroscopy is essential (Fig. 3a). Carrier doping transfers the spectral weight of the Mott-gap transition to the Drude component[21,38], enabling carrier-density estimation from the intensity reduction in the Mott-gap transition. Fitting the $R$ and $\varepsilon_2$ spectra (solid lines in Figs. 3b and c, respectively) with two Lorentz oscillators representing transitions to the odd-parity exciton and doublon–holon continuum (blue and yellow broken lines in Fig. 3c, respectively) results in the purple broken lines shown in Figs. 3b,c. The reduction in these two components is assumed to be proportional to the carrier density[38].

Figure 3d shows the time characteristics of the reflectivity changes, $\Delta R(t)/R$, at the reflectivity peak (1.79 eV) caused by an MIR pulse (0.264 eV) for $|E_{\mathrm{MIR}}| = 2.0 - 12.0\ \mathrm{MV/cm}$ in 1.0 MV/cm steps. For $|E_{\mathrm{MIR}}| \leq 4.0\ \mathrm{MV/cm}$, $\Delta R(t)/R$ shows a pulsed response centred at $t = 0\ \mathrm{ps}$. The $-\Delta R(0\ \mathrm{ps})/R$, plotted as circles in Fig. 3e, is proportional to $|E_{\mathrm{MIR}}|^2$ at $|E_{\mathrm{MIR}}| \leq 4.0\ \mathrm{MV/cm}$. Therefore, the observed signals are attributable to coherent 3rd order nonlinear responses associated with the excitonic Floquet state[44]. Because the Floquet state is formed only under an MIR electric field, it is observed as a pulsed response[44-46] (Supplementary Information S3).

In contrast, for $|E_{\mathrm{MIR}}| > 4.0\ \mathrm{MV/cm}$, a response with a finite decay time appears for $-\Delta R(t)/R$, which is attributable to carrier generation via quantum tunnelling processes under the MIR electric field (Fig. 3f). On increasing $|E_{\mathrm{MIR}}|$ beyond $4.0\ \mathrm{MV/cm}$, $-\Delta R(0\ \mathrm{ps})/R$ tends to saturate because the coherent response is disturbed by carrier generation. Notably, $-\Delta R(0.25\ \mathrm{ps})/R$ should be used to investigate the $|E_{\mathrm{MIR}}|$ dependence of the carrier density because the coherent response completely disappears at $t = 0.25$ ps. Figure 3e indicates that $-\Delta R(0.25\ \mathrm{ps})/R$ shows a threshold behaviour, attaining a value of 0.35 at $|E_{\mathrm{MIR}}| \sim 12.0\ \mathrm{MV/cm}$. These signals should reflect carrier generation via the quantum tunnelling processes, the probability of which ($\Gamma$) in 1D Mott insulators can be expressed as follows[34]:

$$\Gamma \propto \exp(-\pi E_{\mathrm{th}}/|E_{\mathrm{MIR}}|),\ \ E_{\mathrm{th}} = \frac{\Delta_{\mathrm{Mott}}}{2e\xi}\,. \tag{1}$$

Here, $E_{\mathrm{th}}$, $\xi$, and $e$ are the threshold electric field, doublon–holon correlation length, and elementary charge, respectively. Using this equation, $-\Delta R(0.25\ \mathrm{ps})/R$ is approximately reproduced, as shown by the purple solid line in Fig. 3e; the used parameter values, $E_{\mathrm{th}} = 13.4\ \mathrm{MV/cm}$ and $\Delta_{\mathrm{Mott}} = 1.76\ \mathrm{eV}$ yield $\xi \sim 6.57$ Å ($\sim 1.68$ sites[41]). To estimate the carrier density $n_{\mathrm{c}}$, the change in $\sigma$ at 0.25 ps should be estimated from $-\Delta R(0.25\ \mathrm{ps})/R$. The sum of doublon and holon density per site, $n_{\mathrm{c}}$, can be approximated as $-\Delta I/2I$, where $I$ represents the sum of the strengths of two Lorentz oscillators (LO1, 2) obtained to reproduce the original $R$ and imaginary part of the dielectric constant $\varepsilon_2$ spectra, and $\Delta I$ is the MIR electric-field-induced change in $I$. The green broken line in Fig. 3b represents the $R$ spectrum calculation when $-\Delta I/I = 0.3$. By back-calculating $-\Delta I/2I$ from $-\Delta R(0.25\ \mathrm{ps})/R$, we obtained the $|E_{\mathrm{MIR}}|$ dependence of $n_{\mathrm{c}}$ as squares (Fig. 3e), which exhibit the same tendency as $-\Delta R(0.25\ \mathrm{ps})/R$. Analysis indicated that $n_{\mathrm{c}}$ reaches 0.25 at $|E_{\mathrm{MIR}}| = 12.0\ \mathrm{MV/cm}$. Further details are provided in Supplementary Information S4.

Importantly, the high density of carriers and expected Mott-insulator melting are reflected in the novel spectral shifts of the HHs. The HH spectra are plotted against $\omega/\Omega$ for the 3rd to 13th order harmonics at $|E_{\mathrm{MIR}}| = 6.0 - 12.0\ \mathrm{MV/cm}$ in Figs. 4a–f and at $|E_{\mathrm{MIR}}| = 4.0 - 6.0\ \mathrm{MV/cm}$ in Extended Data Figs. 3a–f. We fitted each spectrum with a Gaussian profile and determined the frequencies of the $n^{\mathrm{th}}$ order peak structures, $\omega_{\mathrm{peak,n}}$. Figure 4h shows the $|E_{\mathrm{MIR}}|$ dependence of the peak shifts, $(\omega_{\mathrm{peak},n} - n\hbar\Omega)$. At $|E_{\mathrm{MIR}}| \leq 6.0\ \mathrm{MV/cm}$, each peak energy almost coincides with $n\hbar\Omega$. At $|E_{\mathrm{MIR}}| > 6.0\ \mathrm{MV/cm}$, the energies of the 3rd order harmonics are equal to $3\hbar\Omega$, while those of the 5th and higher order harmonics show redshifts with increasing $|E_{\mathrm{MIR}}|$, saturating around $|E_{\mathrm{MIR}}| = 12.0\ \mathrm{MV/cm}$. The redshift magnitude increases with $n$, reaching ~50 meV at the 11th harmonic. The $|E_{\mathrm{MIR}}|$ dependence of these shifts is similar to that of $n_{\mathrm{c}}$ (Fig. 4g), suggesting that the redshifts originate from successive electronic-state changes, i.e., metallisation.

To investigate the relationship between the electronic-state changes and HH shifts, we simulated the dynamics of the half-filled Hubbard model in the Mott regime (see Methods). The time evolution was computed using time-dependent dynamical mean-field theory (tdDMFT)[47], which describes electronic-structure changes with carrier relaxation and scattering processes in strongly correlated systems, providing the time evolutions of the doublon and holon energy levels, single-particle spectra, $n_{\mathrm{c}}$, and antiferromagnetic spin-spin correlation $m_{\mathrm{AFM}}$. The following parameters were used to fit $Sr_2CuO_3$: $U = 2.6\ \mathrm{eV}$, bandwidth $W = 2.08\ \mathrm{eV}$, and bond length $b = 3.9$ Å. The temperature $T$ was set at 260 K, where $\Delta_{\mathrm{Mott}}$ is ~1.5 eV and antiferromagnetic order develops, consistent with the electronic state in $Sr_2CuO_3$. This Mott-insulator state was excited with a Gaussian electric-field pulse centred at $t = 0$ with the frequency $\Omega/2\pi = 63\ \mathrm{THz}$ ($\hbar\Omega = 0.26\ \mathrm{eV}$) and temporal width $\sigma_0 = 63.3\ \mathrm{fs}$ (Figs. 5a–c).

To explain the experimentally observed HH shifts by tdDMFT, we first calculated the integrated HH spectra (Fig. S6), from which the deviations in HH peak energies, $\hbar\omega_{\mathrm{peak},n}$, from $n\hbar\Omega$ were

obtained as a function of $|E_{\mathrm{MIR}}|$ (Fig. 4j). We also evaluated the $|E_{\mathrm{MIR}}|$ dependence of $n_{\mathrm{c}}$ after the pulse (Fig. 4i). These results reproduce the redshifts observed with a sharp increase in $n_{\mathrm{c}}$ shown in Figs. 4g,h. To further pursue the physical origin of this behaviour, we next analysed the sub-cycle evolutions of $n_{\mathrm{c}}$, $m_{\mathrm{AFM}}$, and single-particle spectra (Figs. 5d–f) (Supplementary Information S5). At $|E_{\mathrm{MIR}}| = 6.7$ MV/cm, they remain almost unchanged over time. At $|E_{\mathrm{MIR}}| = 12.0$ and 16.0 MV/cm, $n_{\mathrm{c}}$ increases and $m_{\mathrm{AFM}}$ reduces during the pulse, suggesting an electric-field-induced Mott transition. Correspondingly, the single-particle spectrum varies cycle-by-cycle, the original Mott gap shrinks, and the spectral weight is transferred from the lower to the upper Hubbard band with time. The population in the upper Hubbard band corresponds to the Drude weight in $\sigma(\omega)$. The observed evolution of the single-particle spectrum indicates transient changes in the dynamics of doublons and holons, which affect the sub-cycle radiation processes, eventually causing HH peak shifts (Fig. 4j).

It is noteworthy that HH peak shifts are influenced by both the intensity and phase of successive radiation, which can be explained as follows. Figures 5g-i show sub-cycle radiation intensities, whose profiles beyond the original gap can be associated with the three-step dynamics of doublons and holons[28,29]. At $|E_{\mathrm{MIR}}| = 6.7$ MV/cm, the radiation is nearly periodic and strongest near the pulse centre (Fig. 5g). With stronger fields, the periodicity is violated, and the radiation weight shifts earlier (Figs. 5h,i). At first glance, the suppression of radiation around $t = 0$ appears to contour intuitively against the shrinking gap, likely owing to the reduction in the coherence of doublon–holon dynamics with progress in metallisation.

After identifying the relevant time window, we evaluated the radiation phase to examine the conditions for constructive and destructive interference between successive sub-cycle radiations. The radiation phase around a given time $t = t_{\mathrm{p}}$ is defined as $\mathrm{Arg}[J(\omega, t_{\mathrm{p}})]$, where $J(\omega, t_{\mathrm{p}})$ is the current within the interval $t \in (t_{\mathrm{p}} - T_{\mathrm{hp}}/2,\ t_{\mathrm{p}} + T_{\mathrm{hp}}/2)$, and $J(\omega) = \sum_l J(\omega,\ t_{\mathrm{p}} + lT_{\mathrm{hp}})$, where $T_{\mathrm{hp}} = \pi/\Omega$ and $l$ is an integer indicating the time domain of each window. In Figs. 5j–l, we plot the difference of $\mathrm{Arg}[J(\omega, t)]$ from a reference time $t_i = -73.2$ fs; $\Delta\mathrm{Arg}[J(\omega, t)] \equiv \mathrm{Arg}[J(\omega, t)] - \mathrm{Arg}[J(\omega, t_{\mathrm{i}})]$ at $\omega = n\Omega$, and $\omega = \omega_{\mathrm{peak},n}$ ($n = 3$ and 9) for each half cycle. The results for $n = 3 - 11$ are shown in Fig. S9. At $|E_{\mathrm{MIR}}| = 6.7$ MV/cm, the phases for $\omega = n\Omega$ and $\omega = \omega_{\mathrm{peak},n}$ are almost equal, and they vary only slightly from cycle to cycle. At $|E_{\mathrm{MIR}}| = 12.0$ and 16.0 MV/cm, similar behaviour is observed for $n = 3$, which corresponds to in-gap radiation. In contrast, for $n \geq 7$, a pronounced difference arises between $\omega = n\Omega$ and $\omega = \omega_{\mathrm{peak},n}$. The radiations at $\omega = \omega_{\mathrm{peak},n}$ exhibit smaller phase variations when their intensities are strong; they constructively accumulate compared with those at $\omega = n\Omega$. Notably, at $|E_{\mathrm{MIR}}| = 16.0$ MV/cm, the radiation phase at $\omega = n\Omega$ becomes nearly flat for $t > 0$; therefore, a suppression in HH peak shifts is expected. However, this tendency was not observed because of the previously mentioned reduction in radiation intensity caused by the decoherence effect in the metallic state. This result highlights the importance of both phase modulation and decoherence in shaping HH spectra. The distinct behaviour of the HH

signals between $n = 3$ and $n \geq 7$ (Figs. 4j, S7, and S9) can be attributed to their distinct physical origins; the HHG at $n = 3$ originates from non-resonant processes within the gap in the perturbative regime and from the intraband current when sufficient charge carriers are generated, whereas that at $n \geq 7$ arises from the doublon–holon three-step mechanism. The HHG at $n = 5$ represents an intermediate case. The radiations from two types of mechanisms at $n = 3$ are both expected to be enhanced as the Mott gap shrinks, while their phase should remain unaffected, consistent with the experimental results.

**Discussion**

HH peak shifts have been observed in gases and solids. In gases, HH peaks are blue-shifted at strong electric fields beyond the saturation magnitude for optical-field-induced ionisation[48,49]. In solids, HH shifts depend upon the carrier-envelope phase (CEP) of the excitation pulse[8,50]. For example, the combination of long scattering time, Dirac dispersion, and short-pulse excitation enables the generation of tunable non-integer harmonics from the surface state of the topological insulator $Bi_2Te_3$[50]. In these phenomena, the sub-cycle dynamics of charge carriers are modified by controlling *the shape of the excitation pulse*.

On the other hand, the HH-shift mechanism observed in $Sr_2CuO_3$ differs from that reported previously, likely owing to the sub-cycle modification of charge dynamics under strong electron correlation, which depends sensitively on the carrier density and progress of nonequilibrium electronic-state changes. Intuitively, this mechanism may be interpreted as a form of the Doppler effect, which connects the redshift in the energy level of a doublon–holon pair with that of the HHs. If the system is in a time-periodic state, the radiation phase at a frequency $\omega_r$ changes by $\pi - \omega_{\mathrm{r}} T_{\mathrm{hp}}$ for each half cycle, which results in constructive interference at $\omega_{\mathrm{r}} = n\Omega$ ($n$: odd number). Next, we consider a simplified situation where the modification in doublon–holon dispersion can be approximated as a uniform level shift by $\Delta\epsilon$ per $T_{\mathrm{hp}}$. Within the three-step model[29], the additional phase shift for the radiation from doublon–holon recombination is approximately $(\Delta\epsilon/\hbar)(t_{\mathrm{r}} - t_{\mathrm{c}})$, where $t_{\mathrm{r}}(t_{\mathrm{c}})$ is the recombination (creation) time of the doublon–holon pair. For constructive interference, the additional phase must be compensated with the frequency deviation from the integer harmonic, $\Delta\omega_{\mathrm{r}} = \omega_{\mathrm{r}} - n\Omega$. Thus, the Mott-gap reduction $(\Delta\epsilon < 0)$ associated with metallisation leads to HH redshifts $(\Delta\omega_{\mathrm{r}} < 0)$. In general, electronic-structure changes depend on the material and excitation conditions, which can be characterised by the deformation pattern of the HH spectra. Unlike other CEP-dependent HHG phenomena reported previously, the present mechanism of HH redshift is insensitive to CEP (Supplementary Information S5) and does not require long scattering times.

These results reveal that the HH spectrum and sub-cycle electronic-structure changes during the nonequilibrium phase transition of strongly correlated systems are closely connected. The Mott insulator state and corresponding Hubbard model are prototypical examples. Other examples involve

various types of orders, including superconductivity, (anti)ferromagnetism, and orbital order, where nonthermal phase transitions are induced by light or electric fields. This leads to an intriguing open question that should be addressed with a combination of systematic HHG experiments and advanced nonequilibrium many-body theories: what types of fingerprints do these diverse nonequilibrium phase transitions leave in the HH spectra? Our study highlights HHG as a promising probe for assessing the real-time evolution of quantum materials, paving the way for future developments in nonequilibrium spectroscopy.

**Acknowledgements**

We thank Mr. Z. Zhong, Mr. Y. Suzuki, and Ms. M. Xu for their assistance in constructing the optical setups and Dr. S. Kito for his support in X-ray diffraction measurements to determine the crystallographic orientation of single crystals. We also thank Prof. M. Eckstein for enlightening discussions. This work was partly supported by a Grant-in-Aid for Scientific Research from the Japan Society for the Promotion of Science (JSPS) (Project Numbers: JP21H04988, JP21H05017, JP24H00191, JP25K07235, JP25K17961), CREST (JPMJCR1661), Japan Science and Technology Agency, Iketani Science and Technology Foundation (0371180-A), and Toyota Riken Scholar. D.S. was supported by Support for Pioneering Research Initiated by Next Generation of Japan Science and Technology Agency (JST SPRING) (Grant Number: JPMJSP2108).

**Author contributions**

R.I., D.S., T.M., and H.O. built the experimental setups of high harmonic spectroscopy and pump probe reflection spectroscopy. R.I. and D.S. performed the measurements. T.I. prepared the sample. Y.M. performed the DMFT calculations. H.O. coordinated the study. The manuscript was written by R.I., Y.M., and H.O. with inputs from the other authors.

**Competing interests**

The authors declare no competing interests.

**Additional information**

**Supplementary information** is available for this paper at https://doi.org/.

**Correspondence and requests for materials** should be addressed to H.O. or Y.M.

**Reprints and permissions information** is available at.

## Methods

### Sample preparations

Single crystals of $Sr_2CuO_3$ were grown via the laser-diode-heated floating-zone method[51] using the traveling solvent technique[39]. The initial composition of the solvent with SrO:CuO = 40 mol%:60 mol% was determined from the phase diagram of the SrO–CuO system[52]. A mixture of argon (60 vol%) and oxygen (40 vol%) flowed through the growth chamber at a rate of 100 $cm^3$/min. The growth rate was 1 mm/h.

### Polarised reflectivity spectrum measurements

The polarized reflectivity ($R$) spectrum of $Sr_2CuO_3$ along the $b$ axis was measured using a Fourier transform infrared spectrometer (0.08–1.2 eV) and a spectrometer with a grating monochromator (0.46–6.2 eV), both of which were equipped with an optical microscope. The optical conductivity ($\sigma$) spectra and the imaginary part of dielectric constant ($\varepsilon_2$) spectra were calculated from the $R$ spectrum using the Kramers–Kronig transformation. All the optical measurements were performed on a clean surface along the *bc*-plane obtained by cleaving the single crystal. To prevent sample degradation, the single crystal was put in a vacuum during the measurements.

### HH spectrum measurements

Schematics of the HH spectrum measurements are shown in Extended Data Fig. 1. A Ti:sapphire regenerative amplifier (RA) with a photon energy of 1.55 eV, temporal width of 35 fs, output fluence of 7 mJ, and repetition rate of 1 kHz was used as the laser source. The RA output was used as input into an optical parametric amplifier (OPA1) to generate signal and idler lights through an optical parametric process; these outputs were input into a 1 mm-thick second-order nonlinear optical crystal, z-cut GaSe, to generate an MIR pulse with a photon energy of 0.263 eV via a differential-frequency generation process. The signal and idler lights used to generate the MIR pulse were cut using long-pass filters (LPF1 and LPF2) to ensure that they were not introduced into the sample. The maximum electric-field amplitude of the MIR pulse was controlled using two MIR wire-grid polarisers (WG1 and WG2), and a third polariser (WG3) was used to ensure good light polarisation along the *b*-axis of $Sr_2CuO_3$. The temporal and spectral widths of the MIR pulses were ~220 fs and 22 meV, respectively (Supplementary Information S1).

To measure the HH spectra in the normal-reflection configuration, a soda-lime glass substrate deposited with indium tin oxide (ITO) was used as a beam splitter (BS) for MIR and HH light. A broadband wire-grid polariser (WG4), applicable in the near-IR (NIR) to visible (VIS) region, was used to resolve the polarisation of the HH light. Two fiber spectrometers, an NIR spectrometer (Lambda Vision) and a VIS spectrometer (QE-Pro, Ocean optics), were used to measure the HH spectra in the 0.70–1.5 eV and 1.4–4.0 eV regions, respectively. The measured HH spectra were

modified by the optical properties of the optics shown in Extended Data Fig. 1 and the detection sensitivity of spectrometer, both of which depend on the wavelength of the HH lights. Therefore, the HH spectra should be corrected. By placing a standard light source, a halogen tungsten lamp (DH-3 PLUS, Ocean Optics), at the sample position and comparing the obtained spectrum with the spectrum of the standard light source, we evaluated the correction factor, which was used to correct all the HH spectra.

**MIR pump-visible reflectivity probe measurements**

Schematics of the MIR pump-visible reflectivity probe measurements are shown in Extended Data Fig. 2. The laser source and generation method for the MIR pump pulses were identical to those used for the HH spectrum measurements. The photon energy was 0.264 eV. A part of the RA output was input into another OPA2, from which the probe pulse (1.79 eV) was generated. The temporal and spectral widths of the visible pulses were 55 fs and 55 meV, respectively, while those of the MIR pulses were ~170 fs and 24 meV, respectively (Supplementary Information S1). The delay time of the probe pulse relative to the pump pulse was varied using a mechanical stage installed in the probe beam path. The MIR-pump and VIS-probe pulses were polarised parallel to the *b*-axis of $Sr_2CuO_3$. To reduce the effects of intensity fluctuations of the probe pulses, a part of each probe pulse was extracted by a BS, and its intensity was measured as a reference with photodetector 2 (PD2). The intensity of the probe pulse reflected from the sample was measured as a signal with photodetector 1 (PD1) and normalised by the reference using a boxcar integrator.

**DMFT calculations**

We analysed the time evolution of the single-band Hubbard model to understand the origin of the redshifts of HH peaks. Under an electric field, the Hubbard model can be expressed as follows:

$$\hat{H}(t) = -t_{\mathrm{hop}} \sum_{\langle i,j \rangle} e^{i\phi_{ij}(t)} \hat{c}_{i\sigma}^{\dagger} \hat{c}_{j\sigma} + U \sum_i \hat{n}_{i\uparrow} \hat{n}_{i\downarrow},$$

where $\hat{c}_{i\sigma}^{\dagger}$ is the creation operator for an electron with spin $\sigma$ at site $i$, $\langle i,j \rangle$ indicates a pair of neighbouring sites, $\hat{n}_{\mathrm{i}\sigma} = \hat{c}_{i\sigma}^{\dagger} \hat{c}_{i\sigma}$, $t_{\mathrm{hop}}$ is the hopping parameter, and $U$ is the onsite Coulomb repulsion. The effect of electric fields is included via a Peierls phase, $\Phi_{\mathrm{ij}}(t) = -\mathrm{e}\boldsymbol{A}(t) \cdot \boldsymbol{r}_{ij}$. Here, $\boldsymbol{A}(t)$ is the vector potential, which is related to the electric field $\boldsymbol{E}(t)$ as $\boldsymbol{E}(t) = -\partial_t \boldsymbol{A}(t)$ and $\boldsymbol{r}_{ij}$ is the position operator from site $j$ to site $i$. Here, $U$ (2.6 eV), the bandwidth ($W =$ 2.08 eV), and the bond length ($b =$ 3.9 Å) were set to be consistent with $Sr_2CuO_3$, unless otherwise mentioned. The temperature was set as $T =$ 260 K.

We solved this model using a nonequilibrium extension of the DMFT[47], a powerful numerical method for studying strongly correlated systems both in and out of equilibrium. DMFT is based on Green's function formalism, where the nonequilibrium Green's function $G_i(t,t') = -i\langle T_C \hat{c}_i(t) \hat{c}_i^{\dagger}(t') \rangle$ is defined on the L-shaped contour, *C*. In DMFT, the original lattice model is

mapped to an effective impurity model to fully incorporate dynamic local correlations. This method is suitable for systems in the thermodynamic limit and can explain the Mott physics, reformulation of electronic structures, and relaxation or scattering processes. In this study, we used the non-crossing approximation as the impurity solver within the DMFT self-consistency loop; the code was based on the open-source library Nessi[53].

For simulations, we used the Hubbard model on a Bethe lattice to reduce computational cost and ensure systematic analysis. This setup corresponds to the application of an electric field along the body diagonal of a general hypercubic lattice. Previous studies have shown that DMFT dynamics are generally insensitive to lattice geometry, and similar behaviour is expected in other lattices. We set the pump pulse to a Gaussian pulse as follows:

$$A(t) = \frac{E_0}{\Omega} F_{\mathrm{Gauss}}(t - t_0, \sigma_0) \sin[\Omega(t - t_0) + \phi_{\mathrm{CEP}}],$$

where $F_{\mathrm{Gauss}}(t, \sigma_0) = \exp[-t^2/2{\sigma_0}^2]$. We set $\hbar\Omega = 0.26$ eV, $t_0 = 0$ fs, $\sigma_0 =$ 63.3 fs, and $\phi_{\mathrm{CEP}} = 0$, and simulated from $t_{\mathrm{min}} = -253.2$ fs up to $t_{\mathrm{max}} = 253.2$ fs, unless otherwise mentioned. Within tdDMFT, we evaluated various physical observables to characterise the dynamics of the system. The HHG spectrum $I_{\mathrm{HHG}}(\omega)$ is computed from the current $J(t)$ using $I_{\mathrm{HHG}}(\omega) = |\omega J(\omega)|^2$, obtained via the Fourier transform of $J(t)$. In practice, to reduce noise in the Fourier transform due to the finite time range of the simulation, we apply a Gaussian window $F_{\mathrm{Gauss}}(t - t_0, \sigma')$. Here, $\sigma'$ is chosen to be wider than $\sigma_0$ but shorter than $t_{\mathrm{max}} - t_0$. In practice, we set $\sigma' =$ 101.3 fs to satisfy this condition. Notably, the results were found to be insensitive to the choice of $\sigma'$.

To resolve the radiation information within the pump cycle, we conducted sub-cycle analysis. Specifically, we applied a windowed Fourier transform $J(\omega, t_{\mathrm{p}}) = \int dt e^{i\omega t} F_{\mathrm{window}}(t - t_{\mathrm{p}}) J(t)$, which provides an emission profile around $t_{\mathrm{p}}$, where $F_{\mathrm{window}}(t)$ is a window function centred at $t = 0$. For the sub-cycle intensity spectrum in Figs. 5g–i, we set $F_{\mathrm{window}}(t) = F_{\mathrm{Gauss}}(t - t_{\mathrm{p}}, \sigma_{\mathrm{p}})$ with $\sigma_p =$ 1.5 fs and evaluated $I_{\mathrm{HHG}}(\omega, t_{\mathrm{p}}) \equiv |\omega J(\omega, t_{\mathrm{p}})|^2$. To extract the phase information of the emission cycle-by-cycle in Figs. 5j–l, we set $F_{\mathrm{window}}(t)$ as $F_{\mathrm{box}}((t - t_{\mathrm{p}})/T_{\mathrm{hp}}, 0.2)$, which covers a half cycle of the pulse $t \in (t_{\mathrm{p}} - T_{\mathrm{hp}}/2, t_{\mathrm{p}} + T_{\mathrm{hp}}/2)$. A detailed description of $F_{\mathrm{box}}$ is provided in Supplementary Information S5.

The single-particle spectrum represents the electronic states that are accessible by adding or removing one electron to or from the system, and its occupation can be measured by photoemission experiments. In practice, they can be expressed as follows:

$$A(t_{\mathrm{p}},\omega) = -\frac{1}{\pi}\mathrm{Im}\left[\int dtdt' e^{i\omega(t-t')} S(t)S(t') G^{R}(t+t_{\mathrm{p}}, t'+t_{\mathrm{p}})\right],$$

$$N(t_{\mathrm{p}},\omega) = -\frac{i}{2\pi}\int dtdt' e^{i\omega(t-t')} S(t)S(t') G^{<}(t+t_{\mathrm{p}}, t'+t_{\mathrm{p}}),$$

where $G^{\mathrm{R}}$ and $G^{<}$ are the retarded and lesser parts of the (on-site) Green's function, respectively, and $S(t)$ is a Gaussian window function representing the probe pulse in the photoemission experiment. In our analysis, we set the width of $S(t)$ to 5 fs to capture the sub-cycle dynamics. These functions are local and averaged over the sites. Notably, the occupation in the upper Hubbard band corresponds to doublon formation. Thus, the doublon density was evaluated by integrating the occupation over the upper Hubbard band, as follows:

$$n_{\mathrm{d}}(t_{\mathrm{p}}) \equiv \frac{\int_0^{\infty} d\omega N(t_{\mathrm{p}},\omega)}{\int_{-\infty}^{\infty} d\omega A(t_{\mathrm{p}},\omega)}.$$

Because the number of holons equals the number of doublons in this system, the total carrier density per site, $n_{\mathrm{c}}$, is $2n_{\mathrm{d}}(t)$. The antiferromagnetic spin–spin correlation $m_{\mathrm{AFM}}$ is defined as $n_{\uparrow,\mathrm{A}} - n_{\uparrow,\mathrm{B}}$, where A and B represent two sublattices in the bipartite lattice.

**Data availability**

The data of this study are available from the corresponding author upon reasonable request.

**Code availability**

The codes are available from the corresponding author upon reasonable request.

**References**


1. Corkum, P. B. Plasma perspective on strong field multiphoton ionization. *Phys. Rev. Lett.* **71**, 1994–1997 (1993).
2. For a recent review of HHG in solids, see Heide, C., Kobayashi, Y., Haque, S. R. U., & Ghimire, S. Ultrafast high-harmonic spectroscopy of solids. *Nat. Phys*. **20**, 1546–1557 (2024).
3. Paul, P. M. et al. Observation of a train of attosecond pulses from high harmonic generation. *Science* **292**, 1689–1692 (2001).
4. Corkum, P. B. & Krausz, F. Attosecond science. *Nat*, *Phys*. **3**, 381-387 (2007).
5. Niikura, H. et al. Sub-laser-cycle electron pulses for probing molecular dynamics. *Nature* **417**, 917–922 (2002).
6. Krausz, F. & Ivanov, M. Attosecond physics. *Rev. Mod. Phys.* **81**, 163–234 (2009).
7. Ghimire, S. et al. Observation of high-order harmonic generation in a bulk crystal. *Nat*. *Phys*. **7**, 138-141 (2011).
8. Schubert, O. et al. Sub-cycle control of terahertz high-harmonic generation by dynamical Bloch oscillations. *Nat. Photon.* **8**, 119–123 (2014).
9. Luu, T. T. et al. Extreme ultraviolet high-harmonic spectroscopy of solids. *Nature* **521**, 498–502 (2015).
10. Liu, H. et al. High-harmonic generation from an atomically thin semiconductor. *Nat*. *Phys*. **13**, 262–265 (2017).
11. Yoshikawa, N., Tamaya, T. & Tanaka, K. High-harmonic generation in graphene enhanced by elliptically polarized light excitation. *Science* **356**, 736–738 (2017).
12. Lv, Y-Y. et al. High-harmonic generation in Weyl semimetal β-$WP_2$ crystals. *Nat*. *Commun*. **12**, 6437 (2021).
13. Vampa, G. et al. All-Optical Reconstruction of Crystal Band Structure. *Phys*. *Rev*. *Lett*. **115**, 193603 (2015).
14. Borsch, M. et al. Super-resolution lightwave tomography of electronic bands in quantum materials. *Science* **370**, 1204-1207 (2020).
15. Uzan-Narovlansky A. J. et al. Observation of light-driven band structure via multiband high-harmonic spectroscopy. *Nat*. *Photon*. **16**, 428–432 (2022).
16. Luu, T. T. & Wörner H. J. Measurement of the Berry curvature of solids using high-harmonic spectroscopy. *Nat*. *Commun*. **9**, 916 (2018).
17. Uzan-Narovlansky, A. J. et al. Observation of interband Berry phase in laser-driven crystals. *Nature* **626**, 66–71 (2024).
18. Uchida, K. Pareek, V. Nagai, K. Dani, M. & Tanaka, K. Visualization of two-dimensional transition dipole moment texture in momentum space using high-harmonic generation spectroscopy. *Phys*. *Rev*. *B* **103**, L161406 (2021).

19. Imada, M. Fujimori, A. &Tokura, Y. Metal-insulator transitions. *Rev*. *Mod*. *Phys*. **70**, 1039-1263 (1998).
20. Cavalleri, A. et al. Femtosecond structural dynamics in $VO_2$ during an ultrafast solid-solid phase transition. *Phys*. *Rev*. *Lett*. **87**, 237401 (2001).
21. Okamoto, H. et al. Photoinduced Metallic State Mediated by Spin-Charge Separation in a One-Dimensional Organic Mott Insulator. *Phys*. *Rev*. *Lett*. **98**, 037401 (2007).
22. Kübler, C. et al. Coherent Structural Dynamics and Electronic Correlations during an Ultrafast Insulator-to-Metal Phase Transition in $VO_2$. *Phys*. *Rev*. *Lett*. **99**, 116401 (2007).
23. Matsubara, M. et al. Ultrafast Photoinduced Insulator-Ferromagnet Transition in the Perovskite Manganite $Gd_{0.55}Sr_{0.45}MnO_3$ *Phys*. *Rev*. *Lett*. **99**, 207401 (2007).
24. Yusupov, R. et al. Coherent dynamics of macroscopic electronic order through a symmetry breaking transition. *Nat*. *Phys*. **6**, 681–684 (2010).
25. Okamoto, H. et al. Photoinduced transition from Mott insulator to metal in the undoped cuprates $Nd_2CuO_4$ and $La_2CuO_4$. *Phys*. *Rev*. *B* **83**, 125102 (2011).
26. Mayer, B. et al. Tunneling breakdown of a strongly correlated insulating state in $VO_2$ induced by intense multiterahertz excitation. *Phys*. *Rev*. *B* **91**, 235113 (2015).
27. Li, X. et al. Keldysh Space Control of Charge Dynamics in a Strongly Driven Mott Insulator. *Phys*. *Rev*. *Lett*. **128**, 187402 (2022).
28. Murakami, Y., Eckstein, M. & Werner, P. High-Harmonic Generation in Mott Insulators. *Phys*. *Rev*. *Lett*. **121**, 057405 (2018).
29. Murakami, Y., Takayoshi, S., T. Koga, A. & Werner, P. High-harmonic generation in one-dimensional Mott insulators. *Phys*. *Rev*. *B* **103**, 035110 (2021).
30. Uchida, K. et al. High-Order Harmonic Generation and Its Unconventional Scaling Law in the Mott-Insulating $Ca_2RuO_4$. *Phys*. *Rev*. *Lett*. **128**, 127401 (2022).
31. Tancogne-Dejean, N. Sentef, M. A. & Rubio, A. Ultrafast Modification of Hubbard *U* in a Strongly Correlated Material: Ab initio High-Harmonic Generation in NiO. *Phys*. *Rev*. *Lett*. **121**, 097402 (2018).
32. Silva, R. E. F. Blinov, I. V. Rubtsov, A. N. Smirnova, O. & Ivanov, M. High-harmonic spectroscopy of ultrafast many-body dynamics in strongly correlated systems. *Nat*. *Photon*.**12**, 266-270 (2018).
33. Valmispild, V. N. et al. Sub-cycle multidimensional spectroscopy of strongly correlated materials. *Nat*. *Photon*. **18**, 432–439 (2024).
34. Oka, T. Nonlinear doublon production in a Mott insulator: Landau-Dykhne method applied to an integrable model. *Phys*. *Rev*. *B* **86**, 075148 (2012).
35. Liu, M. et al. Terahertz-field-induced insulator-to-metal transition in vanadium dioxide metamaterial. *Nature* **487**, 345 (2012).

36. Yamakawa, H. et al. Mott transition by an impulsive dielectric breakdown. *Nat. Mater.* **16**, 1100 (2017).
37. Ogata, M. & Shiba, H. Bethe-ansatz wave function, momentum distribution, and spin correlation in the one-dimensional strongly correlated Hubbard model. *Phys*. *Rev*. *B* **41**, 2326 (1990).
38. Eskes, H. & Andrzej, M. O. Two Hubbard Bands: Weight Transfer in Optical and One-Particle Spectra. *Phys*. *Rev*. *Lett*. **73**, 1279 (1994).
39. Motoyama, N. Eisaki, H. & Uchida, S. Magnetic Susceptibility of Ideal Spin 1 /2 Heisenberg Antiferromagnetic Chain Systems, $Sr_2CuO_3$ and $SrCuO_2$. *Phys*. *Rev*. *Lett*. **76**, 3212 (1996).
40. Ogasawara, T. et al. Ultrafast Optical Nonlinearity in the Quasi-One-Dimensional Mott Insulator $Sr_2CuO_3$. *Phys*. *Rev*. *Lett*. **85**, 2204 (2000).
41. Ono, M. et al. Linear and nonlinear optical properties of one-dimensional Mott insulators consisting of Ni-halogen chain and CuO-chain compounds. *Phys*. *Rev*. *B* **70**, 085101 (2004).
42. Xia, P. et al. Nonlinear propagation effects in high harmonic generation in reflection and transmission from gallium arsenide. *Opt*. *Exp*. **26**, 29393-29400 (2018).
43. Neufeld, O. Podolsky, D. & Cohen, O. Floquet group theory and its application to selection rules in harmonic generation. *Nat*. *Commun*. **10**, 405 (2019).
44. Yamakawa, T. Miyamoto, T Sakai, D. & Okamoto, H. Dynamical aspects of excitonic Floquet states generated by a phase-locked mid-infrared pulse in a one-dimensional Mott insulator. *New J. Phys*. **25**, 093044 (2023).
45. Zhou, S. et al. Pseudospin-selective Floquet band engineering in black phosphorus., *Nature* **614**, 75-80 (2023).
46. Shan, J-Y. et al. Giant modulation of optical nonlinearity by Floquet engineering. *Nature* **600**, 235–239 (2021).
47. Aoki, H. et al. Nonequilibrium dynamical mean-field theory and its applications. *Rev*. *Mod*. *Phys*. **86**, 779 (2014).
48. Shin, H. J. et al. Generation of Nonadiabatic Blueshift of High Harmonics in an Intense Femtosecond Laser Field. *Phys*. *Rev*. *Lett*. **83**, 2544 (1999).
49. Bian, X-B. & Bandrauk, A. D. Spectral Shifts of Nonadiabatic High-Order Harmonic Generation. *Appl*. *Sci*. **3**, 267 (2013).
50. Schmid, C. P. et al. Tunable non-integer high-harmonic generation in a topological insulator. *Nature* **593**, 385–390 (2021).
51. Ito, T. et al. Laser-diode-heated floating zone (LDFZ) method appropriate to crystal growth of incongruently melting materials. *J. Cryst. Growth* **363**, 264-269 (2013).
52. Hwang, N. M. Roth, R. S. & Rawn, C. J. Phase Equilibria in the Systems SrO-CuO and SrO-1/2$Bi_2O_3$. *J. Am. Cer. Soc.* **73**, 2531-2533 (1990).
53. Schüler, M. et al. NESSi: The Non-Equilibrium Systems Simulation package. *Comput*. *Phys*.

*Commun*. **257**, 107484 (2020).

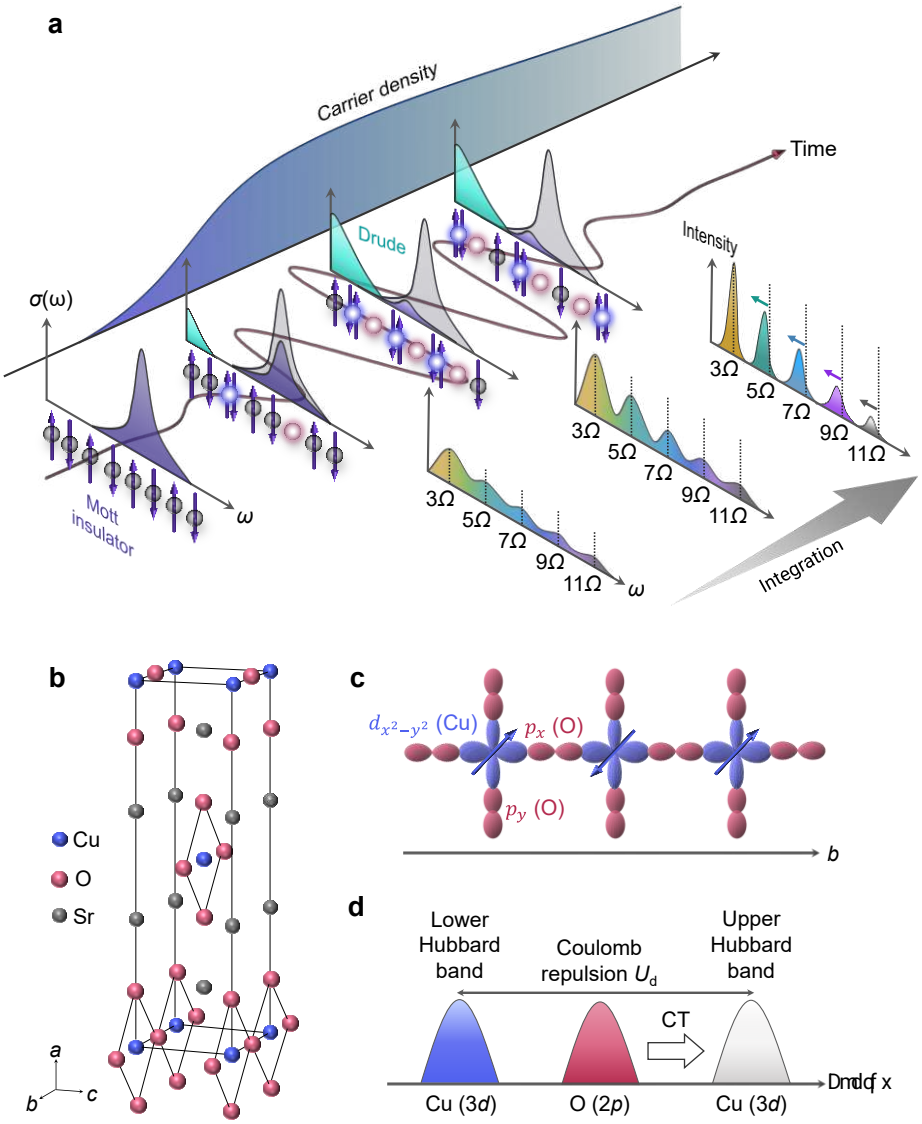



**Fig. 1 | High-harmonic generation (HHG) during a Mott insulator–metal transition induced by a mid-infrared (MIR) pulse in a one-dimensional (1D) cuprate, $Sr_2CuO_3$. a**, Schematics of the time characteristics of the electronic-state changes and HHG under a strong MIR electric field. The spectral weight of the original Mott-gap transition is transferred to the Drude component by doublon and holon creation. Accumulated HH spectra can shift to lower energies with progress in metallisation. **b**, Crystal structure of $Sr_2CuO_3$. **c**, 1D electronic state consisting of the $d_{x^2-y^2}$ orbital of Cu and $p$ orbital of O. **d**, Electronic structure of $Sr_2CuO_3$. The lowest electronic transition is the charge transfer (CT) transition from the $O-2p$ band to $Cu-3d$ upper Hubbard band; its energy is denoted by $\Delta_{Mott}$ in the text.

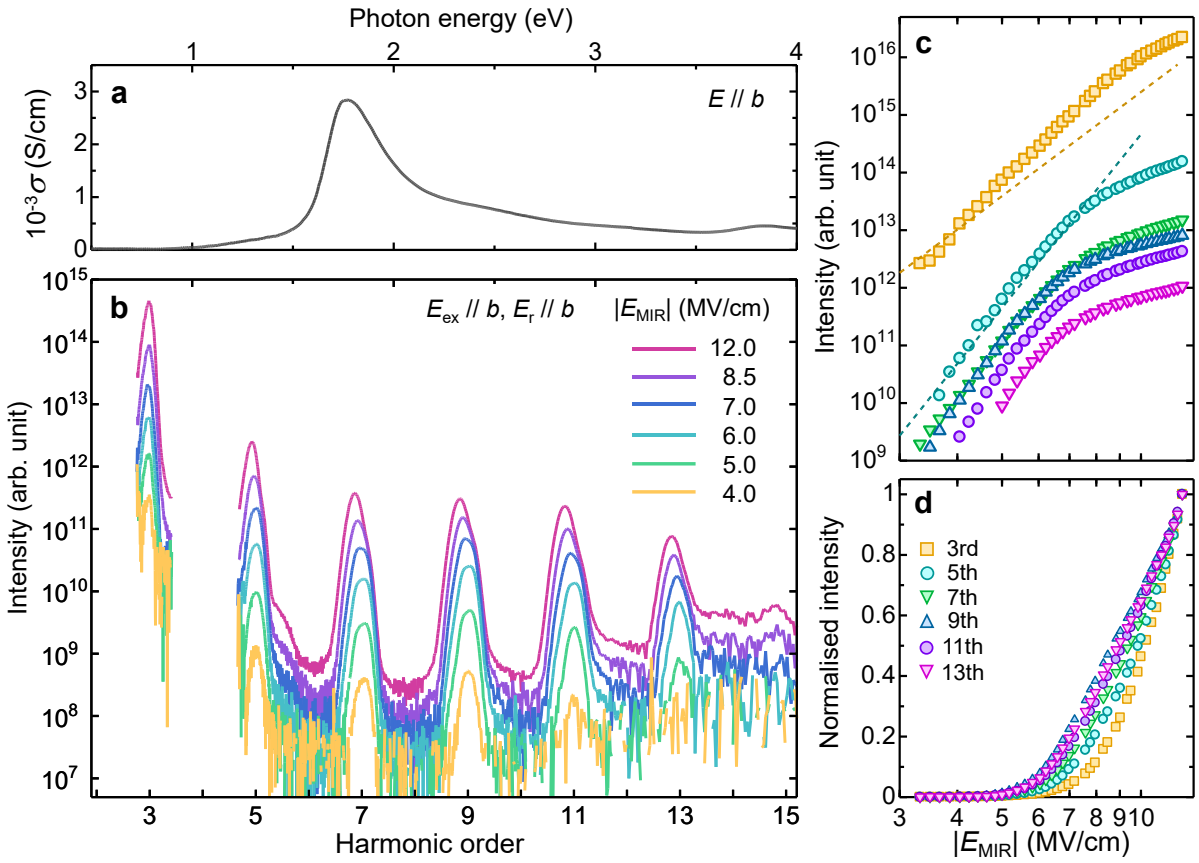



**Fig. 2 | HHG properties as a function of the MIR electric-field amplitude $|E_{\mathrm{MIR}}|$ in $Sr_2CuO_3$. a**, Spectrum of optical conductivity $\sigma(\omega)$ with the electric field of lights, $E$, parallel to the $b$-axis ($E//b$). **b**, Spectra of HHs with the electric field of lights $E_{\mathrm{r}}//b$ obtained by the irradiation of the MIR pump pulse (0.263 eV) with the electric field of lights $E_{\mathrm{ex}}//b$. **c**, **d** $|E_{\mathrm{MIR}}|$ dependence of the integrated intensities of HHs: (**c**) log–log and (**d**) semi-log plots. The yellow (green) broken line in **c** shows the relation $I_{3\mathrm{HG}} \propto |E_{\mathrm{MIR}}|^6$ ($I_{5\mathrm{HG}} \propto |E_{\mathrm{MIR}}|^{10}$).

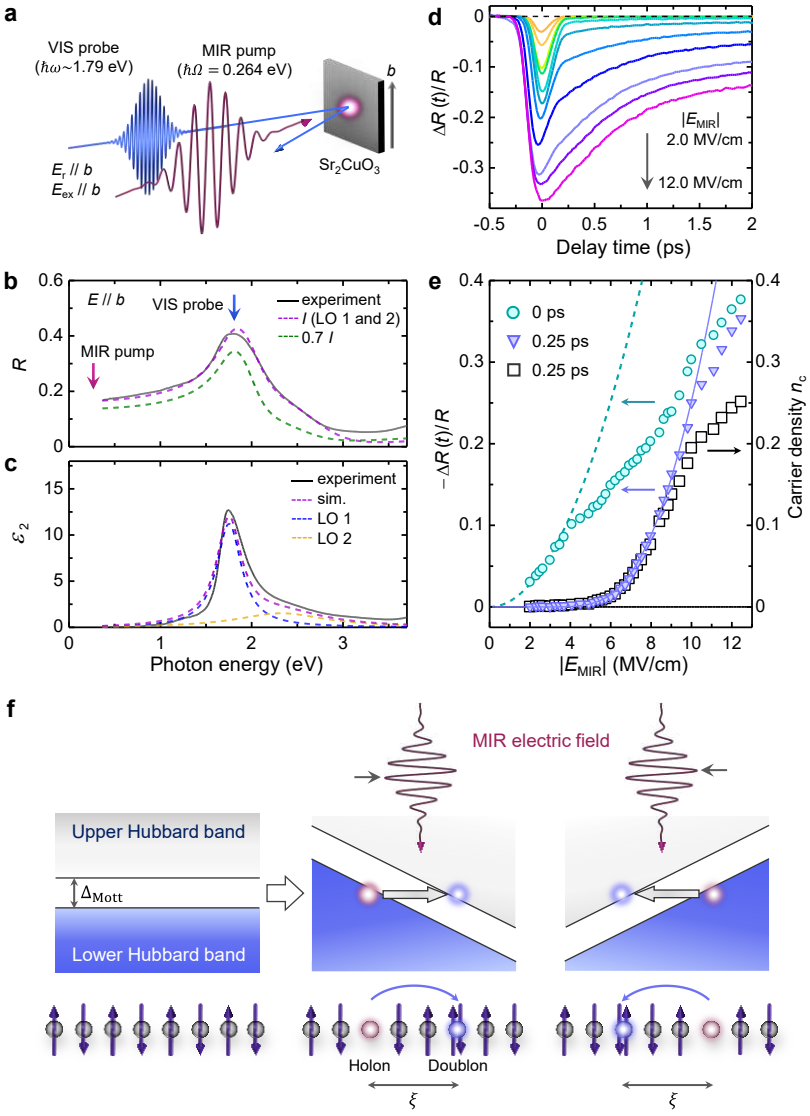



**Fig. 3 | MIR pump-visible reflectivity probe measurements to evaluate the carrier density in $Sr_2CuO_3$. a**, Experimental setup. The arrows show the pump and probe pulse energies. **b**, **c,** Spectra of the (**b**) reflectivity $R$ and (**c**) imaginary part of the relative dielectric constant, $\varepsilon_2$. The purple broken lines in (**b**) and (**c**) show the spectra simulated using two Lorentz-oscillators (LO 1 and 2) represented by the blue and yellow broken lines, respectively, in **c**. The green broken line in **b** is the simulated spectrum for the intensity reduction $(-\Delta I/I)$ required for the total oscillator strength $I$ to be 0.3. **d**, Time characteristics of the reflectivity changes $-\Delta R(t)/R$ for $|E_{\mathrm{MIR}}| = 2-12$ MV/cm in 1 MV/cm steps. **e**, $|E_{\mathrm{MIR}}|$ dependence of $-\Delta R(t)/R$ at $t = 0$ and 0.25 ps (circles and triangles, respectively) and the carrier density $n_c$ at $t = 0.25$ ps (squares). The light-blue and purple broken lines show the relations $-\Delta R(t)/R \propto |E_{\mathrm{MIR}}|^2$ and $-\Delta R(t)/R \propto \Gamma$ in equation (1), respectively. **f**, Schematics of doublon–holon pair creations via quantum tunnelling processes by the MIR electric field.

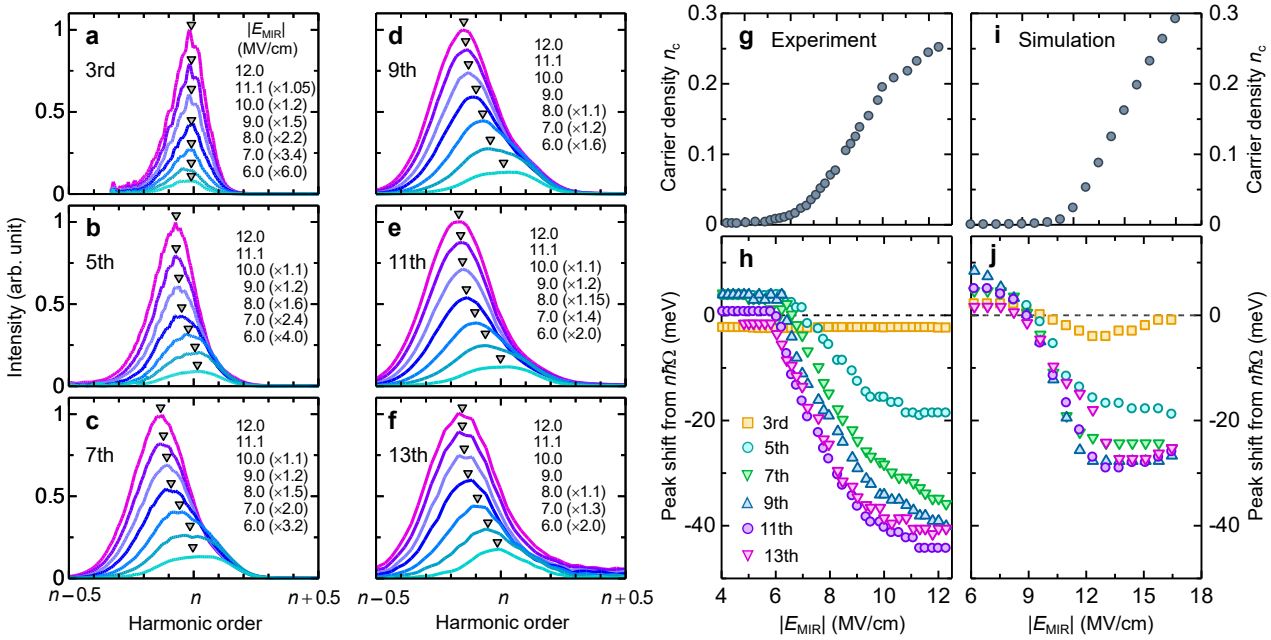



**Fig. 4 | MIR electric-field dependence of the HH spectral shifts in $Sr_2CuO_3$. a–f**, Spectra of 3rd to 13th order harmonics for $|E_{\mathrm{MIR}}| = 6.0 - 12.0$ MV/cm. Triangles show the peak energies (central positions) of each HH spectrum determined by spectral fitting with the Gaussian shape. **g**, $|E_{\mathrm{MIR}}|$ dependence of $n_{\mathrm{c}}$ (the same as the squares in Fig. 3**e**). **h**, $|E_{\mathrm{MIR}}|$ dependence of the HH peak shifts from $n\hbar\Omega$ evaluated from the HH spectra in **a**–**f**. **i**, **j** $|E_{\mathrm{MIR}}|$ dependence of (**i**) $n_{\mathrm{c}}$ and the (**j**) HH peak shifts from $n\hbar\Omega$ evaluated by the DMFT simulation shown in Fig. 5.

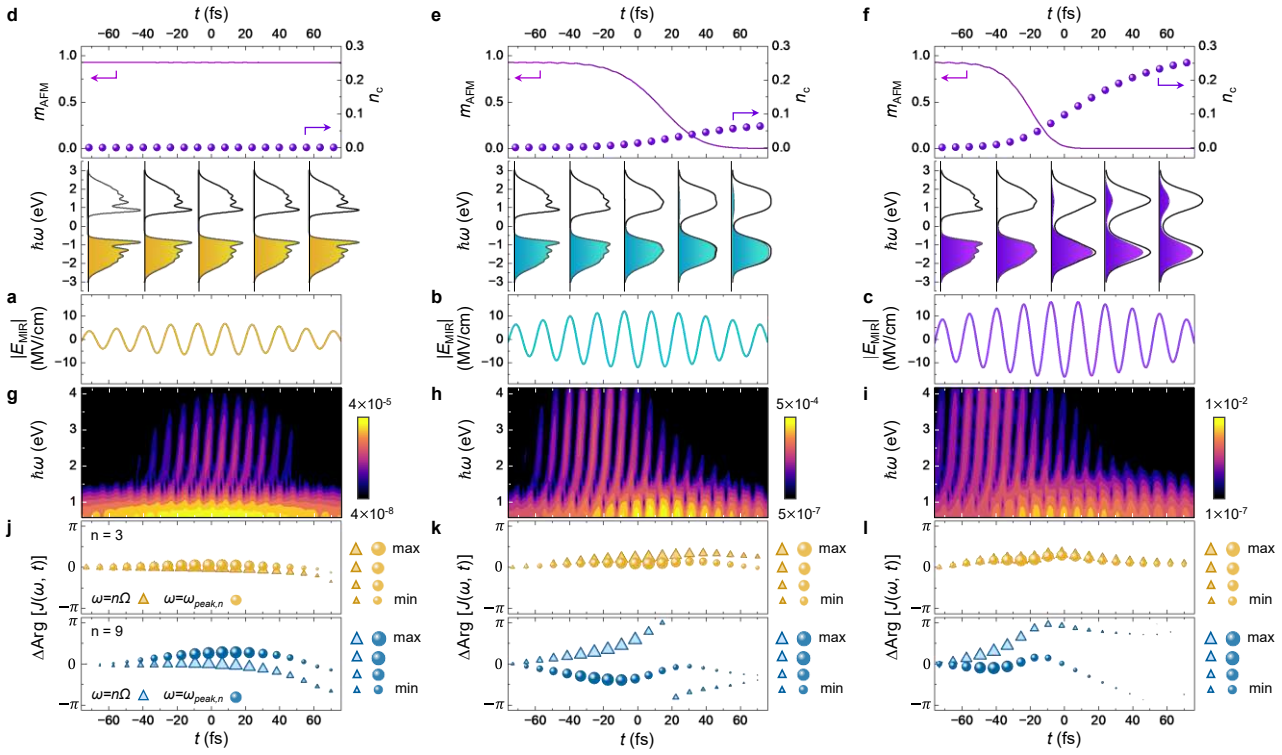
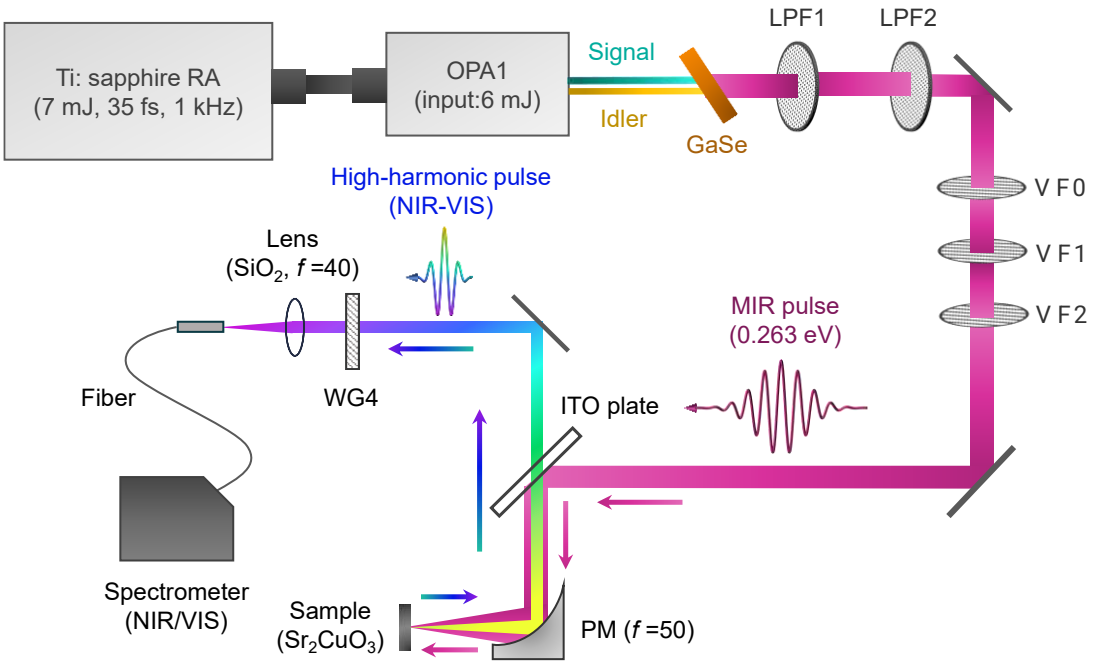
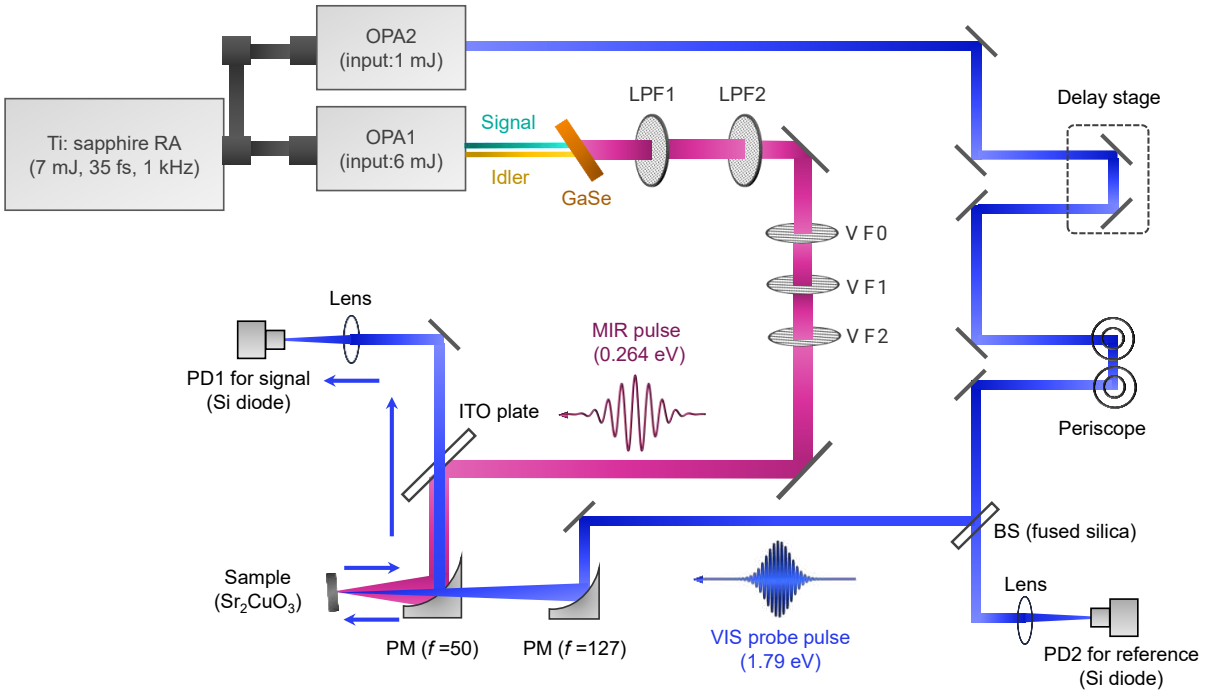


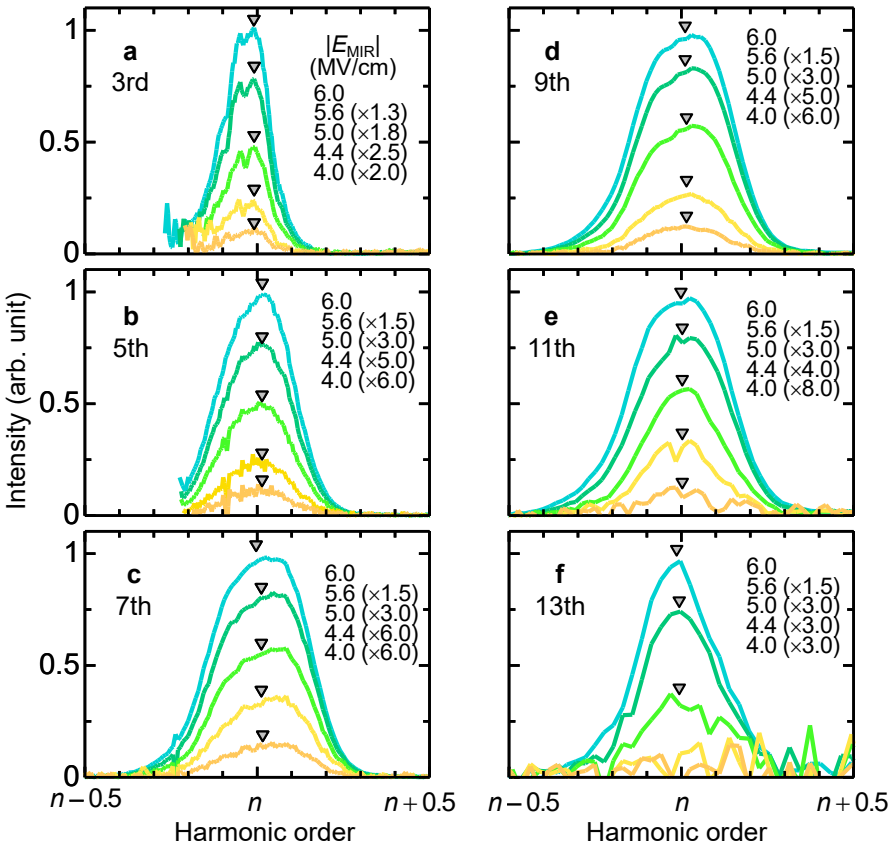

**Fig. 5 | Simulations of HHG in Mott insulators with DMFT. a–c,** Electric-field waveforms of pump pulses with the frequency $\Omega/2\pi = 63$ THz. **d–f,** Upper panels: Antiferromagnetic spin–spin correlation $m_{\mathrm{AFM}}$ and carrier density $n_{\mathrm{c}}$ as a function of $t$. Lower panels: Changes in electronic structure along the electric field of the pump pulse as a function of $t$. Single-particle spectra are shown in solid lines and the filled regimes indicate their occupation. **g–i**, Sub-cycle radiation spectra as a function of $t$. Logarithmic radiation intensity values are indicated by colors defined in the color bar located in the right of each panel. **j–l**, Changes in the phases of sub-cycle radiation, $\Delta\mathrm{Arg}[J(\omega,t)]$, at $\omega = n\Omega$ and $\omega = \omega_{\mathrm{peak},n}$ for $n = 3$ and 9. The size of a marker indicates the intensity of the corresponding radiation. $|E_{\mathrm{MAX}}| = 6.7$ MV/cm in **a**, **d**, **g**, and **j**, $|E_{\mathrm{MAX}}| = 12.0$ MV/cm in **b**, **e**, **h**, and **k**, and $|E_{\mathrm{MAX}}| = 16.0$ MV/cm in **c**, **f**, **i**, and **l**.




**Extended Data Fig. 1: Schematic diagram of HH spectrum measurements.** LPF1 and LPF2 are long-pass filters which are transparent only at the wavelength longer than 3000 and 3500 nm, respectively. PM is a parabolic mirror, the focus length of which is expressed by $f$ (mm). WG1-3 and WG4 are wire-grid polarizers for the MIR region and NIR-VIS region, respectively.




**Extended Data Fig. 2: Schematic diagram of MIR pump-VIS reflectivity probe measurements.** LPF1 and LPF2 are long-pass filters which are transparent only at the wavelength longer than 3000 and 3500 nm, respectively. PM is a parabolic mirror, the focus length of which is expressed by $f$ (mm). WG1-3 are wire-grid polarizers for the MIR region. BS is a beam splitter. PD1 and PD2 are photodetectors (Si diode).




**Extended Data Fig. 3: MIR electric-field dependence of spectral shifts of HHs in $Sr_2CuO_3$ at the lower electric fields.** Spectra of 3rd-13th harmonics for $|E_{MIR}|$ of 4.0 to 6.0 MV/cm. Triangles show peak energies (central positions) of each HH spectrum determined by the spectral fittings with the Gaussian shape.

## Supplementary Files

This is a list of supplementary files associated with this preprint. Click to download.

- SM202583final.pdf